AIAA JOURNAL
Vol. 48, No. 4, April 2010

Frequency-Domain Linearized Euler Model for Turbomachinery Noise Radiation Through Engine Exhaust

Andrea Iob* and Renzo Arina†
Politecnico di Torino, 10129 Torino, Italy
and
Claudia Schipani‡
Avio R&D, 10040 Rivalta di Torino, Italy

DOI: 10.2514/1.J050084

A numerical model for the exhaust noise radiation problem is presented. In the model, it is assumed that an incoming wave is propagating through the exhaust nozzle, or the fan duct, and radiating outside. The near-field propagation is based on the solution of the linearized Euler equations in the frequency domain: for each wave number, a linearized Euler problem is solved using a finite element method on unstructured grids for arbitrarily shaped axisymmetric geometries. The frequency-domain approach enables the suppression of the Kelvin–Helmholtz instability waves. Moreover, each single calculation, limited to a single frequency, is well suited to the exhaust noise radiation problem in which the incoming wave can be treated as a superposition of elementary duct modes. To reduce the memory requirements, a continuous Galerkin formulation with linear triangular and quadrangular elements is employed and the global matrix inversion is performed with a direct solver based on a parallel memory distributed multifrontal algorithm for sparse matrices. The acoustic near field is then radiated in the far field using the formulation of Ffowcs Williams and Hawkings. Numerical calculations for a validation test case, the Munt problem, and two turbomachinery configurations are compared with analytical solutions and experimental data.

I. Introduction

ALTHOUGH in the last decade aircraft engine noise emissions have been considerably reduced, more efforts to achieve further reduction are necessary to meet the more and more stringent environmental targets. Although recent research programs brought significant progress in reducing both the turbomachinery noise generation and the radiation of noise from the intake, there is still a lack of knowledge about the exhaust noise radiation problem and the need to develop accurate models for its prediction. This problem represents a challenge for computational aeroacoustics, due to the fact that radiated sound propagates through the shear layers separating the core, bypass, and freestream fields.

In this paper, a mathematical model of propagation and radiation of turbomachinery noise through the engine exhaust is presented. The aim of the present work is to provide a model able to efficiently predict the acoustic behavior of the engine exhaust so that it can be used to improve turbomachinery aeroacoustics design. In the model it is assumed that an incoming harmonic duct mode is propagating through the exhaust nozzle, or the fan duct, and radiating at infinity as a small perturbation of a steady mean flowfield; therefore, entropy fluctuations and viscous effects are negligible. Under these assumptions, the acoustic propagation is governed by the linearized Euler equations (LEE) in the near field. The nonuniform mean flowfield is a solution of the steady Reynolds averaged Navier–Stokes equations. The far-field radiation occurs in a region where the mean flowfield is essentially uniform; therefore, the far-field solution can be obtained using an integral formulation like the Ffowcs Williams and Hawkings (FW-H) method or the Kirchhoff approach. For the type of problems of interest in this work, the two approaches are equivalent. The FW-H method has been adopted because of the experience acquired in previous studies, in which the FW-H numerical tool was extensively tested.

Both the LEE and the FW-H formulation are solved in the frequency domain. In the frequency domain the time variation of the acoustic variables is assumed to be harmonic, with the frequency response equal to the frequency of the incoming modal wave acting as the sound source. The solution of the LEE in the frequency domain enables the suppression of the temporal growth of the instability waves, known as the Kelvin–Helmholtz instabilities, which may obscure the acoustic solution in the time-domain calculations [1,2]. For a given frequency, the system of algebraic equations resulting after the numerical discretization in space must be assembled and solved globally. The matrix inversion could be solved by means of an iterative technique. However it has been shown that iterative techniques are equivalent to pseudo-time-integration methods and lead to the occurrence of the instability wave solutions [3]. To overcome this problem, a direct method for the inversion of the global matrix must be adopted. Direct methods have larger memory requirements, but the solution is not affected by Kelvin–Helmholtz instabilities. The frequency-domain approach has several advantages for the problem of interest in this paper. The solution of each harmonic mode composing the incoming wave can be obtained by a single matrix inversion; after that, the overall solution is reconstructed in the time domain by an inverse Fourier transform. Both steps are performed with efficient computational techniques; therefore, for signals characterized by few harmonic components, as in the case of turbomachinery tonal noise, the computational time required by a frequency-domain approach is smaller compared to the one necessary for a time-domain computation. Moreover, the frequency-domain approach makes it easier to impose the natural boundary conditions of lining acoustic components [4].

Several frequency-domain solvers for the LEE have been proposed, both with structured [2,5] or unstructured meshes [3,6]. For arbitrary geometries, as in the case of turbomachinery exhaust noise, the latter approach makes it easier to build the mesh. In the present model, the LEE, written in the frequency domain, are solved on an unstructured mesh with a finite element method (FEM), a

Received 23 July 2009; revision received 13 November 2009; accepted for publication 29 November 2009.

*Research Assistant, Dipartimento di Ingegneria Aeronautica e Spaziale, Corso Duca degli Abruzzi 24; andrea.iob@polito.it. Member AIAA.
†Associate Professor, Dipartimento di Ingegneria Aeronautica e Spaziale, Corso Duca degli Abruzzi 24; renzo.arina@polito.it. Member AIAA.
‡Research Engineer, Via I Maggio 99, 10040 Rivalta di Torino; Claudia.Schipani@aviogroup.com. Member AIAA.

natural approach to unstructured grids. The FEM is based on a continuous Galerkin discretization with linear triangular and quadrangular elements. To achieve a higher precision order, the discontinuous Galerkin approach would be more appropriate, but it is extremely memory-expensive, as shown in Rao and Morris [3], leading in the case of a frequency-domain solution of a complex geometry to prohibitive memory requirements. Moreover, to further reduce the memory issue, the global system is solved with a direct method based on a parallel memory distributed multifrontal algorithm for sparse matrices [7]. The perfectly matched layer (PML) technique for the nonreflecting far-field boundary conditions is implemented [8].

In the remainder of this paper, the model and numerical results are presented. In Sec. II, the numerical model for axisymmetric geometries is presented. For each modal frequency, the LEE are written in a form including only radial and axial derivatives. In Sec. III, numerical results are presented. To validate the propagation model, as a first step, the numerical calculations are compared with respect to the analytical solution of the Munt problem [9]. Then the propagation and radiation of noise through two realistic turbofan engine exhaust configurations is studied, and the numerical calculations are compared with the experimental data obtained within the framework of the European Union (EU) project known as Turbomachinery Noise Radiation Through the Engine Exhaust (TURNEX).[§] Results are presented for both the near-field propagation and the far-field angular directivity radiation pattern and compared with experimental results.

II. Wave Propagation Model

A. Near Field: Linearized Euler Equations

1. Definition of Duct Modes

The problem involves the propagation of tonal noise inside an axisymmetric nozzle of a turbofan engine with hard walls in the presence of jet flow. The incident wave can be represented as a sum of harmonic modes with angular frequency ω. Each harmonic mode can be further decomposed into a sum of elementary spatial modes called duct modes [10]. Each duct mode can be written as follows:

$$p(r,\theta,t)=\sum_{m=0}^{\infty}\sum_{\mu=0}^{\infty}a_{m\mu}\mathrm{Re}(\hat{p}_{m\mu}(r)e^{I(m\theta+\omega t+\Phi)}) \tag{1}$$

where the indices (m,μ) identify, respectively, the azimuthal mode and the radial mode; $a_{m\mu}$ are weighting coefficients, by means of which an arbitrary distribution can be decomposed; and Φ is the phase of the mode. Defined as the hub-tip ratio $\lambda=r_{\mathrm{hub}}/r_{\mathrm{tip}}$, the radial shape of a mode propagating in an annular duct with hard walls and uniform mean flow is given by the relation

$$\hat{p}_{m\mu}(r)=J_m\left(\frac{\alpha_r r}{r_{\mathrm{tip}}}\right)+Q^{\lambda}_{m\mu}Y_m\left(\frac{\alpha_r r}{r_{\mathrm{tip}}}\right) \tag{2}$$

where $\alpha_r=\alpha_r(m,\mu,\lambda)$ and $Q^{\lambda}_{m\mu}=Q(m,\mu,\lambda)$ are the successive paired roots of the system:

$$\begin{cases}J'_m(\alpha_r)+QY'_m(\alpha_r)=0,\\ J'_m(\lambda\alpha_r)+QY'_m(\lambda\alpha_r)=0\end{cases} \tag{3}$$

In the previous expressions, Eqs. (2) and (3), J_m and Y_m denote the Bessel functions of the first and second kinds of order m, whereas J'_m and Y'_m are their derivatives. It can be shown [10] that the value of the index μ gives the number of pressure nodes in the radial direction.

2. Governing Equations

The propagation of sound waves in a medium with nonuniform mean velocity $\mathbf{U}_0(\mathbf{x})$, neglecting entropy fluctuations and fluid viscosity, is governed by the linearized Euler equations [11]. In cylindrical coordinates these equations can be written as

$$\frac{\partial \boldsymbol{q}}{\partial t}+\tilde{A}\frac{\partial \boldsymbol{q}}{\partial z}+\tilde{B}\frac{\partial \boldsymbol{q}}{\partial r}+\tilde{C}\frac{\partial \boldsymbol{q}}{\partial \theta}+\tilde{D}\boldsymbol{q}=0 \tag{4}$$

where $\boldsymbol{q}=[\rho',u',v',w',p']^T$ is the acoustic perturbation vector. $\tilde{A}$, $\tilde{B}$, and $\tilde{C}$ are the Jacobian matrices of the fluxes, and $\tilde{D}$ contains the mean flow gradients.

Transforming the equations into the frequency domain and introducing the duct modes, Eq. (1), all acoustic perturbation quantities can be written as a sum of harmonic modes:

$$\boldsymbol{q}=\mathrm{Re}(\hat{\boldsymbol{q}}(r,z,\omega)e^{I(m\theta+\omega t)}) \tag{5}$$

Substituting Eq. (5) into Eq. (4), the LEE for a harmonic elementary mode are given by

$$A\frac{\partial \hat{\boldsymbol{q}}}{\partial z}+B\frac{\partial \hat{\boldsymbol{q}}}{\partial r}+C\hat{\boldsymbol{q}}=0 \tag{6}$$

where $\hat{\boldsymbol{q}}=[\hat{\rho},\hat{u},\hat{v},\hat{w},\hat{p}]^T$ and the matrices A, B, and C have the following expressions:

$$A=\begin{bmatrix}u_0 & \rho_0 & 0 & 0 & 0\\ 0 & u_0 & 0 & 0 & \frac{1}{\rho_0}\\ 0 & 0 & u_0 & 0 & 0\\ 0 & 0 & 0 & u_0 & 0\\ 0 & \gamma p_0 & 0 & 0 & u_0\end{bmatrix},\qquad B=\begin{bmatrix}v_0 & 0 & \rho_0 & 0 & 0\\ 0 & v_0 & 0 & 0 & 0\\ 0 & 0 & v_0 & 0 & \frac{1}{\rho_0}\\ 0 & 0 & 0 & v_0 & 0\\ 0 & 0 & \gamma p_0 & 0 & v_0\end{bmatrix}$$

$$C=\begin{bmatrix}I\omega+\nabla\cdot\boldsymbol{U}_0 & \frac{\partial\rho_0}{\partial z} & \frac{\rho_0}{r}+\frac{\partial\rho_0}{\partial r} & \rho_0\frac{Im}{r} & 0\\ -\frac{1}{\rho_0^2}\frac{\partial p_0}{\partial z} & I\omega+\frac{\partial u_0}{\partial z} & \frac{\partial u_0}{\partial r} & 0 & 0\\ -\frac{1}{\rho_0^2}\frac{\partial p_0}{\partial r} & \frac{\partial v_0}{\partial z} & I\omega+\frac{\partial v_0}{\partial r} & 0 & 0\\ 0 & 0 & 0 & I\omega+\frac{v_0}{r} & \frac{Im}{\rho_0 r}\\ 0 & \frac{\partial p_0}{\partial z} & \frac{\gamma p_0}{r}+\frac{\partial p_0}{\partial r} & \gamma p_0\frac{Im}{r} & I\omega+\gamma\nabla\cdot\boldsymbol{U}_0\end{bmatrix} \tag{7}$$

In Eqs. (7), the subscript $(.)_0$ denotes mean flow quantities, m stands for the azimuthal mode of the incoming wave, and ω is the time angular frequency of that wave. It is evident from Eqs. (7) that, to solve the linearized Euler equations, the mean flowfield must be known in advance.

To reduce computational time and memory requirements, the pressure gradients in the momentum equations are neglected. A similar approximation, called gradient term suppression (GTS), is often used to overcome instability problems that prevent convergence of time-domain algorithms for the LEE [12,13]. Although the original GTS approximation suppresses all mean flow gradients, which are likely to be small in the considered subsonic flows, in the present case, being interested in reducing the computational time, only the mean flow gradients in momentum equations that involve density fluctuations are neglected. This allows one to decouple the continuity equation and to solve only momentum and energy equations. The number of total unknowns is thus reduced by a factor of $\mathcal{T}=5/4$, whereas the nonzero terms in the coefficient matrix of the linear system associated with the discretized form of Eqs. (6) is reduced by a factor of $\mathcal{T}^2$. Indeed, a smaller linear system can be solved faster, and, more important, its resolution requires less memory. Density fluctuations are then evaluated from pressure fluctuations using the relation

$$\rho'=p'/c_0^2 \tag{8}$$

where the mean flow is assumed to be locally isentropic, and c_0 is the local speed of sound. Density fluctuations are only evaluated on the FW-H integration surface, which is always placed in a region where the mean flow is assumed to be uniform and homoentropic.

If the incident wave is neither harmonic nor a single duct mode (m,μ), it is always possible to decompose it in a sum of harmonic elementary modes. For each mode a linearized Euler system has to be solved and then the solution can be reconstructed as the sum of elementary mode solutions.

[§]Data about TURNEX available online at http://ec.europa.eu/research/transport/projects/article_3697_en.html [retrieved 1 February 2010].

3. Boundary Conditions

When solving the linearized Euler equations in an open domain, a condition at the outer boundaries is required to make the problem well posed. To avoid incoming spurious reflections, a PML boundary condition is used [8,14]. It consists of surrounding the computational domain by an artificial domain, called the absorbing layer, inside which the waves are damped.

The PML formulation for the LEE in cylindrical coordinates can be written as

$$A_{\text{pml}}\frac{\partial \hat{\boldsymbol{q}}}{\partial z}+B_{\text{pml}}\frac{\partial \hat{\boldsymbol{q}}}{\partial r}+C_{\text{pml}}\hat{\boldsymbol{q}}=0 \tag{9}$$

The matrices A_{pml}, B_{pml}, and C_{pml} of Eq. (9) are defined as follows:

$$\begin{aligned} &A_{\text{pml}}=\alpha_r A_{\text{uni}}; \qquad A_{\text{pml}}=\alpha_z B_{\text{uni}};\\ &C_{\text{pml}}=\left(\alpha_z\alpha_r C_{\text{uni}}+\alpha_r\sigma_z\frac{M_0}{c_0(1-M_0^2)}A_{\text{uni}}\right) \end{aligned} \tag{10}$$

where $\alpha_z=(1+\frac{\sigma_z}{I\omega})$, $\alpha_r=(1+\frac{\sigma_r}{I\omega})$, and the matrices A_{uni}, B_{uni}, and C_{uni} are the matrices of Eqs. (7) under the assumption that the mean flow is uniform and parallel to the z axis, that is,

$$A_{\text{uni}}=\begin{bmatrix} u_0 & \rho_0 & 0 & 0 & 0\\ 0 & u_0 & 0 & 0 & \frac{1}{\rho_0}\\ 0 & 0 & u_0 & 0 & 0\\ 0 & 0 & 0 & u_0 & 0\\ 0 & \gamma p_0 & 0 & 0 & u_0 \end{bmatrix},\quad B_{\text{uni}}=\begin{bmatrix} 0 & 0 & \rho_0 & 0 & 0\\ 0 & 0 & 0 & 0 & 0\\ 0 & 0 & 0 & 0 & \frac{1}{\rho_0}\\ 0 & 0 & 0 & 0 & 0\\ 0 & 0 & \gamma p_0 & 0 & 0 \end{bmatrix}$$

$$C_{\text{uni}}=\begin{bmatrix} I\omega & 0 & \frac{\rho_0}{r} & \rho_0\frac{Im}{r} & 0\\ 0 & I\omega & 0 & 0 & 0\\ 0 & 0 & I\omega & 0 & 0\\ 0 & 0 & 0 & I\omega & \frac{Im}{\rho_0 r}\\ 0 & 0 & \frac{\gamma p_0}{r} & \gamma p_0\frac{Im}{r} & I\omega \end{bmatrix} \tag{11}$$

The absorption coefficients σ_z and σ_r have the following expressions:

$$\sigma_z=\sigma_{\max}(1-M_0^2)\left|\frac{z-z_l}{D_z}\right|^{\beta},\qquad \sigma_r=\sigma_{\max}\left|\frac{r-r_l}{D_r}\right|^{\beta} \tag{12}$$

where D_z and D_r are the widths of the absorbing layers in the z and r directions, respectively, and z_l and r_l are the positions of the interfaces between the PML domain and the physical domain. The maximum value of the damping $\sigma_{\max}$ is usually taken as $2c_0/\Delta z$ and the coefficient β is set to 2 [14].

PML boundary condition equations are also used to impose incoming waves at inlet boundaries, where incoming waves should be specified but at the same time outgoing waves should leave the computational domain without reflections. This can be achieved applying the PML equations to the reflected wave [2], which can be expressed as the total acoustic field minus the incoming prescribed acoustic wave:

$$\hat{\boldsymbol{q}}_{\text{re}}=\hat{\boldsymbol{q}}-\hat{\boldsymbol{q}}_{\text{in}} \tag{13}$$

Substituting Eq. (13) into Eq. (11), the equation for the inlet PML domain reads

$$A_{\text{pml}}\frac{\partial \hat{\boldsymbol{q}}}{\partial z}+B_{\text{pml}}\frac{\partial \hat{\boldsymbol{q}}}{\partial r}+C_{\text{pml}}\hat{\boldsymbol{q}}=A_{\text{pml}}\frac{\partial \hat{\boldsymbol{q}}_{\text{in}}}{\partial z}+B_{\text{pml}}\frac{\partial \hat{\boldsymbol{q}}_{\text{in}}}{\partial r}+C_{\text{pml}}\hat{\boldsymbol{q}}_{\text{in}} \tag{14}$$

The $\hat{\boldsymbol{q}}_{\text{in}}$ values for the incoming acoustic wave can be evaluated using the analytical equations for the duct modes, Eq. (1).

Duct walls are assumed to be acoustically rigid; this means that they reflect the acoustic waves. On these boundaries the acoustic normal velocity is imposed equal to zero:

$$\nabla\hat{\boldsymbol{U}}\cdot\boldsymbol{n}=0 \tag{15}$$

where $\hat{\boldsymbol{U}}=[\hat{u},\hat{v},\hat{w}]^T$.

Because the dependence of the acoustic field on θ is known, the problem was reduced from a three- to a two-dimensional one in (r,z). Moreover, by applying an appropriate boundary condition at the z axis, the equations could be solved only for $r\geq 0$. The symmetry boundary condition should impose that the acoustic velocity is aligned with the $r=0$ axis, so that, at that axis, a wall boundary condition type can be applied.

4. Numerical Method

The LEE are discretized using a continuous Galerkin formulation of the FEM. Defining a test function vector space, W, and a domain Ω, the weak form of the LEE problem

$$\mathcal{L}(\hat{\boldsymbol{q}})=A\frac{\partial \hat{\boldsymbol{q}}}{\partial z}+B\frac{\partial \hat{\boldsymbol{q}}}{\partial r}+C\hat{\boldsymbol{q}}=\boldsymbol{F} \tag{16}$$

consists in finding $\hat{\boldsymbol{q}}\in W$ such that

$$a(\hat{\boldsymbol{q}},\hat{\mathbf{r}})-l(\hat{\mathbf{r}})=0\quad\forall\ \hat{\mathbf{r}}\in W \tag{17}$$

where the bilinear form a and the linear form l are defined as

$$a(\hat{\boldsymbol{q}},\hat{\mathbf{r}})=\int_{\Omega}\hat{\mathbf{r}}^t\mathcal{L}(\hat{\boldsymbol{q}})\,\mathrm{d}\Omega \tag{18}$$

$$l(\hat{\mathbf{r}})=\int_{\Omega}\hat{\mathbf{r}}^t\boldsymbol{F}\,\mathrm{d}\Omega \tag{19}$$

The Galerkin finite element approximation of this problem is obtained considering a finite element space, W_h to approximate W, and finding $U_h\in W_h$ such that

$$a(\hat{\boldsymbol{q}}_h,\hat{\mathbf{r}}_h)-l(\hat{\mathbf{r}}_h)=0\quad\forall\ \hat{\mathbf{r}}_h\in W_h \tag{20}$$

For the LEE, this formulation lacks stability. Astley et al. [15] have found that solving the LEE with a standard finite element formulation leads to unstable numerical models with the presence of spurious oscillations in the solutions. A possible stabilization strategy, called the algebraic subgrid-scale stabilized (ASGS) method [16], consists of adding to the left-hand side of Eq. (20) a term of the following form:

$$r(\hat{\boldsymbol{q}}_h,\hat{\mathbf{r}}_h)=\int_{\Omega_e}\mathcal{P}(\hat{\mathbf{r}})^t\tau\mathcal{R}(\hat{\mathbf{r}}_h)\,\mathrm{d}\Omega \tag{21}$$

where e is the eth element of the mesh; τ is a matrix of stabilization parameters; $\mathcal{P}$ is equal to minus the adjoint of the operator $\mathcal{L}$, that is, $\mathcal{P}(\hat{\boldsymbol{q}})=-\mathcal{L}^*(\hat{\boldsymbol{q}})$; and $\mathcal{R}(\hat{\boldsymbol{q}}_h)$ is the residual of the differential equation, that is to say, $\mathcal{L}(\hat{\boldsymbol{q}}_h)-\boldsymbol{F}$. The stabilization matrix has the expression $\tau=\tilde{\tau}M_I$, where M_I is the identity matrix, and $\tilde{\tau}$ is the stabilization parameter proposed by Guasch and Codina [17] for the two-dimensional Helmholtz equation. Preliminary numerical tests have proven that this two-dimensional formulation is also effective for axisymmetric geometries and for the LEE.

The space W_h is chosen to be the vector space formed by linear Lagrangian polynomials defined on the nodes of the elements. Therefore, each Fourier coefficient $\hat{q}_i$ of the acoustic fluctuations can be interpolated using its nodal values so that

$$\hat{q}_i(\mathbf{x})=\sum_{l=1}^{N}d_l\varphi_l(\mathbf{x}) \tag{22}$$

where $\varphi_l(l=1,\ldots,N)$ are the linear Lagrangian polynomials, and d_l are N unknown complex coefficients that represent the nodal values of $\hat{q}_i$. Because the functions $\varphi_l(l=1,\ldots,N)$ are linearly independent, the discrete problem can be stated as finding the coefficients d_l such that

$$[a(\varphi_i, \varphi_l) + r(\varphi_i, \varphi_l)]d_l - l(\varphi_i) = 0 \qquad i = 1, \ldots, N \tag{23}$$

The discrete problem leads to a complex matrix system in which the complex Fourier coefficients of the acoustic fluctuations are the unknowns. This system is solved using the multifrontal massively parallel solver (MUMPS) package [7]. MUMPS uses a direct method based on a multifrontal approach that performs a direct factorization $A = \mathrm{LDL}^T$.

B. Far Field: Ffowcs Williams and Hawkings Formulation

To evaluate the acoustic fluctuations in the far field, the three-dimensional Ffowcs Williams and Hawkings equation is solved [18]. This equation is an exact rearrangement of the Navier–Stokes equations and allows one to determinate the acoustic signal at distant observer locations if the details of the source region are already known. The idea behind this approach is to extend the definition of all fluid-dynamic quantities to the whole domain, as well as to the regions occupied by a body. To do this, the fluid-dynamic quantities are multiplied by the Heaviside function of argument f, $H(f)$, where $f = 0$ defines the surface outside of which the solution is desired:

$$H(f) = \begin{cases} 0 & \text{inside the surface} \\ 1 & \text{outside the surface} \end{cases} \tag{24}$$

The only limitation in the choice of this surface is that it must enclose all the solid bodies contained in the computational domain.

In this work the noise source is only prescribed via a boundary condition on a duct inlet, and so the FW-H formulation can be written in differential form as

$$\left(\frac{\partial^2}{\partial t^2} - c_0^2 \frac{\partial^2}{\partial x_i \partial x_i}\right)(H(f)\rho') = -\frac{\partial}{\partial x_i}(F_i \delta(f)) + \frac{\partial}{\partial t}(Q\delta(f)) \tag{25}$$

where

$$F_i = (\delta_{ij} p + \rho u_i (u_j - v_j)) \frac{\partial f}{\partial x_j} \tag{26}$$

$$Q = (\rho_0 v_i + \rho(u_i - v_i)) \frac{\partial f}{\partial x_i} \tag{27}$$

As stated earlier, a prime denotes a perturbation from the freestream condition denoted by the subscript $(.)_0$. The fluid velocities are u_i, whereas v_i represent the velocities of the surface f. The total density and pressure are given by $\rho = \rho_0 + \rho'$ and $p = p_0 + p'$, respectively.

The FW-H formulation is used for the propagation of the acoustic fluctuations in the far field. It is reasonable to assume that in the far field the mean flow is uniform. When the mean flow is aligned with the z axis, the motion of the surface is governed by $f = f(z + w_0 t)$, where w_0 is the constant velocity describing the motion. Applying a Galilean transformation to Eq. (25), the frequency-domain solution of the FW-H equation can be written in a Cartesian-coordinate system as [19]

$$H(f)c_0^2 \hat{\rho}(\mathbf{y}, \omega) = -\int_{f=0} I\omega \hat{Q}(\boldsymbol{\xi}, \omega) G(\mathbf{y}; \boldsymbol{\xi})\, \mathrm{d}s - \int_{f=0} \hat{F}_i(\boldsymbol{\xi}, \omega) \frac{\partial G(\mathbf{y}; \boldsymbol{\xi})}{\partial y_i}\, \mathrm{d}s \tag{28}$$

where G is the appropriate Green function, $\boldsymbol{\xi}$ are the surface coordinates, and $\mathbf{y}$ are the observer coordinates. In the numerical implementation, the source terms $\hat{Q}$ and $\hat{F}_i$ are obtained by evaluating the functions Q and F_i in the time domain and then applying the Fourier transform. The time-domain expressions of F_i and Q after the coordinate transformation are

$$F_i = [\delta_{ij}(p_0 + p') + (\rho_0 + \rho')(u_i' - w_0\delta_{3i})(u_j' + w_0\delta_{3j}) + \rho_0 w_0^2 \delta_{3i}\delta_{3j}]\hat{n}_j \tag{29}$$

$$Q = [(\rho_0 + \rho')(u_i' + w_0\delta_{3i}) - \rho_0 w_0 \delta_{3i}]\hat{n}_i \tag{30}$$

where $\hat{n}_i$ is the outward directed unit normal vector. The surface velocities v_i have been replaced by $-w_0\delta_{3i}$; this implies that the mean flow is in the positive direction (or, equivalently, that the surface moves in the negative direction) when $w_0 > 0$. The u_i' are the same fluid velocities of Eq. (25); therefore, they do not contain the motion of the mean flow, $w_0\delta_{3i}$. Under the assumption that the mean flow is subsonic, the Green function for Eq. (28) could be obtained applying a Prandtl–Glauert transformation to the three-dimensional free space Green function; this leads to

$$G = -(1/4\pi R\beta) e^{-Ik(R/\beta - Mz/\beta^2)} \tag{31}$$

where the wave number is defined as $k = \omega/c_0$, $R = \sqrt{(x-\xi)^2 + (y-\eta)^2 + (z-\zeta)^2/\beta^2}$, $M = w_0/c_0$, and $\beta = \sqrt{1 - M^2}$.

The near-field calculations are performed only in the (x, z) plane. Because the FW-H model is fully three dimensional, the acoustic field must be reconstructed over the whole three-dimensional integration surface. The θ dependence of the acoustic variables is given by Eq. (5); therefore, over an axisymmetric surface, the acoustic field is given by

$$\hat{\boldsymbol{q}}(x, y, z, \omega) = \hat{\boldsymbol{q}}(r, z, \omega)|_{\theta=0} e^{Im\theta} \tag{32}$$

with $y/x = \tan\theta$.

III. Results

A. Model Validation: Munt Problem

To validate the numerical model, the acoustic diffraction by a sound wave propagating out of a rigid semi-infinite cylindrical duct (Fig. 1) is studied. The radius of the cylinder is equal to $r_1 = 1.212$ m, and both surfaces of the duct, inner and outer, are rigid. The duct contains a uniform axial mean flow of density ρ_2, Mach M_2, and speed of sound c_2. In the outer region, the flow is also uniform and axial, with density ρ_1, Mach M_1, and speed of sound c_1. There is no shear layer between the two flows; instead, they are separated by a vortex sheet. For this problem, which is called the "Munt problem," the analytical solution proposed by Munt [9] has been subsequently generalized for annular ducts and lined walls [20–22]. Three flow conditions are studied: in the first one the acoustic medium is at rest, herein referred as the no-flow condition, whereas in the others, termed the static-approach and static-cutback conditions, there is a mean velocity inside the duct. The flow properties for each flow condition are given in Table 1.

The computational domain for the near-field calculations extends for $z \in [-2.5\text{ m}; 5.5\text{ m}]$ and for $r \in [0.0\text{ m}; 3.9\text{ m}]$ and is surrounded by vertical and horizontal PML domain with a thickness of 0.7 m, which means that, for a wave with a frequency of 866 Hz, the layers have a thickness of about 1.75 wavelengths. The domain is discretized using a uniform structured grid with 76 elements per meter in both the z and r directions, resulting in a grid with about 250,000 quadrilateral elements. For the FW-H calculation, two different integration surfaces are used. For the no-flow condition, the surface is a cylinder with a radius of 1.24 m, closed in the fore region by a semisphere centered at the duct exit plane. In the aft region, the surface is open and extends to the end of the computational domain, that is, −2.5 m. For the other conditions, the surface is a cylinder with a radius of 1.25 m, open on both sides and extending over the

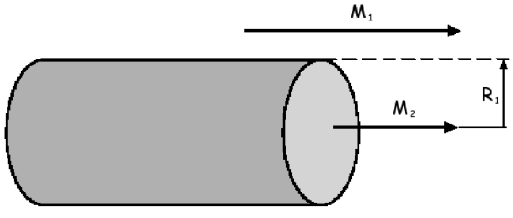

Fig. 1 Circular duct geometry: Munt problem.

Table 1 Circular duct: mean flow properties

	No flow	Static approach	Static cutback
M_1	0.000	0.000	0.000
M_2	0.000	0.447	0.737
c_1, m/s	340.17	340.17	340.17
c_2, m/s	340.17	347.19	349.32
ρ_1, kg/m^3	1.225	1.225	1.225
ρ_2, kg/m^3	1.225	1.177	1.163

entire near-field domain. It is important to note that in the static-approach and static-cutback conditions the surface is not foreclosed; the reason is that the FW-H integration surface must be placed entirely in a uniform flow and, therefore, cannot cross the vortex sheet. The surface is discretized with a grid that is uniform in both the z and θ directions. Because the far-field calculations have a small impact in terms of computational requirements, the number of points per wavelength on the integration surface is always at least equal to, but more often larger than, the corresponding value for the near-field acoustic mesh.

For the no-flow condition, the incoming wave consists of a (m, μ) mode varying harmonically in time with frequency of 956 Hz, corresponding to a dimensionless frequency equal to $kr_1 = 21.4$, and with unit incident intensity. Because the grid has 76 elements per meter, there are about 27 elements per wavelength (EPW). In Fig. 2a, the near-field instantaneous pressure perturbations for the duct mode (0, 1) are reported; the figure shows the contour plot of the real part of the Fourier pressure coefficient, $\mathrm{Re}(\hat{p})$. Figure 2b displays the corresponding sound pressure level (SPL) directivity pattern, describing the field radiated out of the duct. The far-field directivity is evaluated on an arc with the center defined at the center of the duct exit section and a radius equal to $r = 46$ m. Similar results are presented for mode (9, 1) in Figs. 3a and 3b. For all these cases, the agreement between the numerical and the analytical solution is very good.

In the static-approach condition, there is a mean flow velocity inside the duct, with a Mach number equal to 0.447, whereas outside the duct the fluid is at rest. In Figs. 4a and 4b, the instantaneous pressure field and directivity for mode (9, 1), with a frequency of 866 Hz ($kr_1 = 18.99$ and EPW = 30), are presented. Also in this case there is a good agreement with the analytical solution. To have a physical solution, the acoustic pressure must be continuous at the duct lip (Kutta condition). Because the numerical solution is continuous on the mesh nodes, the Kutta condition is naturally satisfied by the numerical model. The vorticity shed from the duct lip can be see in Figs. 5a and 5b, in which the real part of the axial velocity Fourier coefficient is presented.

Figures 6a and 6b show the near- and far-field results for the static-cutback condition. This condition deals with a higher Mach number and a higher frequency. The mean flow velocity inside the duct has a Mach number equal to 0.737, and the frequency of the wave is 1430 Hz ($kr_1 = 31.17$ and EPW = 18). The far-field numerical and analytical results agree reasonably well for this condition.

B. Realistic Exhaust Configurations

As realistic exhaust geometries, the two geometries used in TURNEX are studied. The first geometry is an exhaust referred to as short cowl nozzle, and the second is an exhaust referred to as long cowl nozzle. For the short cowl nozzle geometry, two different flow conditions are considered: in the first one the acoustic medium is at rest (no-flow condition), whereas in the second one there is a mean velocity both inside the bypass duct and the core duct (static-approach condition). Flow properties at the ducts' inlet for each flow condition are given in Table 2. The mean flow computations for the

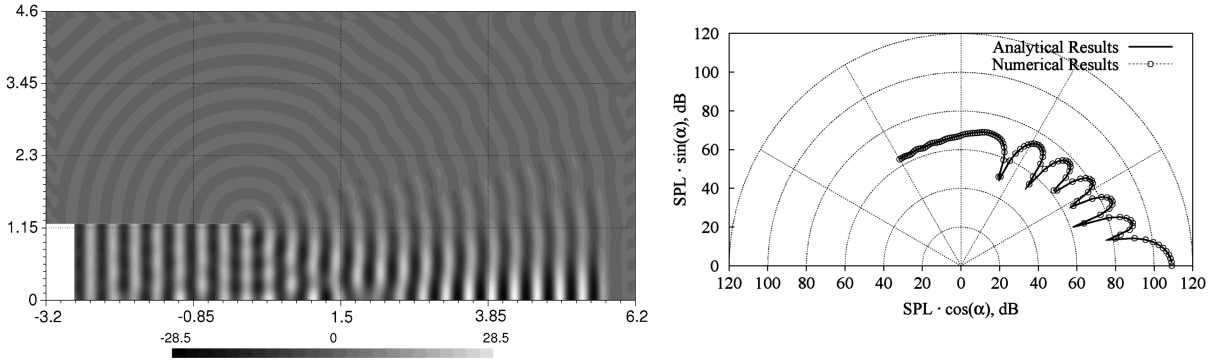

Fig. 2 Circular duct, no-flow condition, mode (0, 1), $f = 956$ Hz, $M_1 = 0.0$, $M_2 = 0.0$: a) near-field solution: real part of Fourier pressure coefficient, [Pa]; and b) far-field solution: SPL directivity.

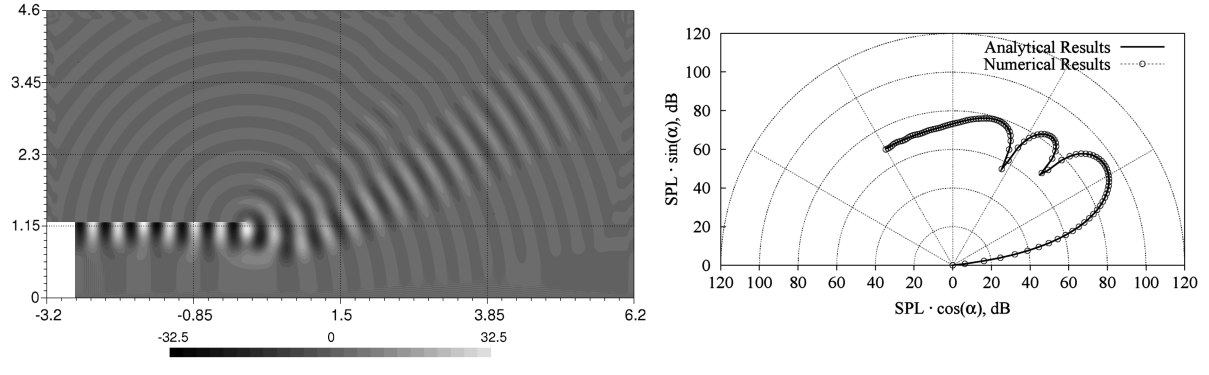

Fig. 3 Circular duct, no-flow condition, mode (9, 1), $f = 956$ Hz, $M_1 = 0.0$, $M_2 = 0.0$: a) near-field solution: real part of Fourier pressure coefficient, [Pa]; and b) Far-field solution: SPL directivity.

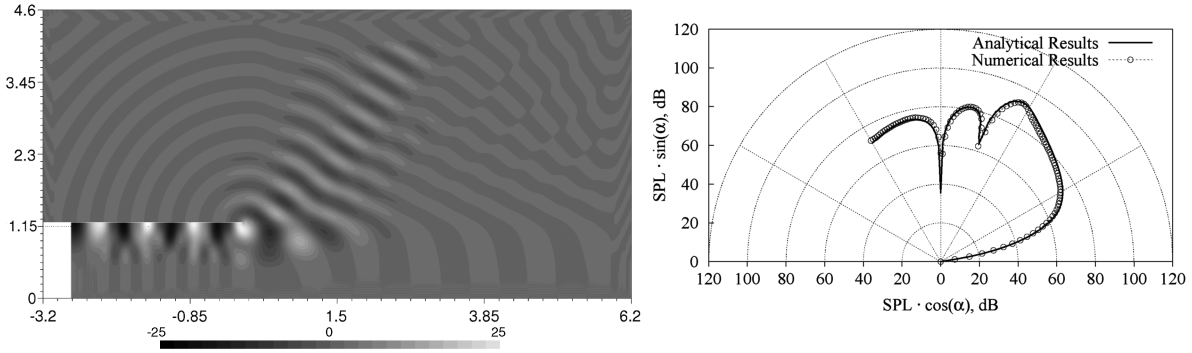

a) b)

Fig. 4 Circular duct, static-approach condition, mode (9,1), $f = 866$ Hz, $M_1 = 0.0$, $M_2 = 0.447$: a) near-field solution: real part of Fourier pressure coefficient, [Pa]; and b) far-field solution: SPL directivity.

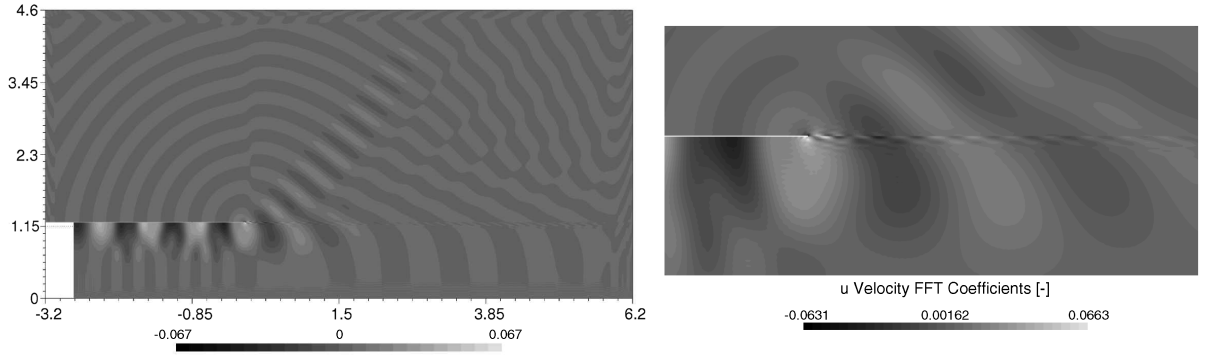

a) b)

Fig. 5 Circular duct, static-approach condition, mode (9, 1), $f = 866$ Hz, $M_1 = 0.0$, $M_2 = 0.447$, real part of Fourier axial velocity coefficient, [m/s], in the near field: a) solution in the whole domain, and b) close-up of the region near the duct lip.

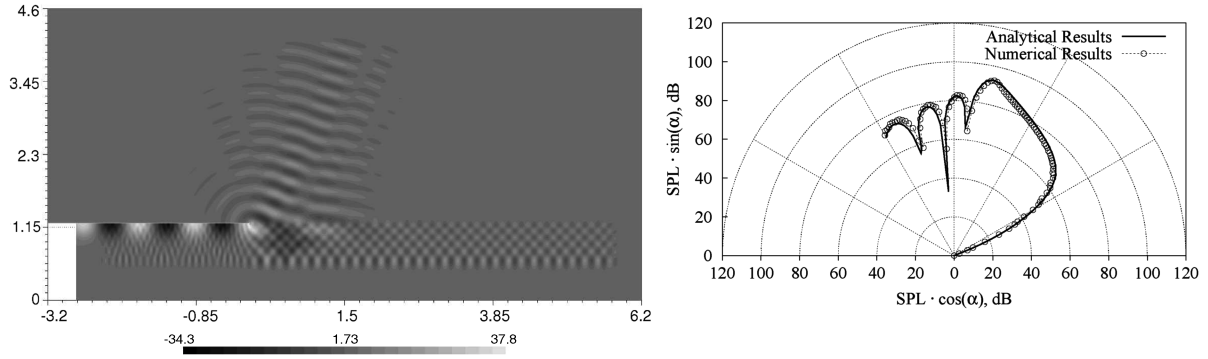

a) b)

Fig. 6 Circular duct, static-cutback condition, mode (21, 1), $f = 1430$ Hz, $M_1 = 0.0$, $M_2 = 0.737$: a) near-field solution: real part of Fourier pressure coefficient, [Pa]; and b) far-field solution: SPL directivity.

static-approach condition were performed at the Middle East Technical University in the framework of TURNEX, solving the Reynolds averaged Navier–Stokes (RANS) equations with a k–ϵ turbulence model. In Fig. 7, the axial velocity contours for the static-approach flow condition are shown. The nodal values of the mean flow on the acoustic mesh are evaluated, interpolating the computational fluid dynamics (CFD) data. Each acoustic node is localized inside the CFD mesh and then the corresponding mean flow values are linearly interpolated from the nodal values of the CFD-mesh element containing the acoustic node. The derivatives of the mean flow are first evaluated on the CFD mesh and then interpolated on the acoustic mesh using the same linear interpolating functions.

The external computational domain for the near-field calculations extends for $z \in [-0.495\text{ m}; 1.2\text{ m}]$ and for $r \in [0.0001\text{ m}; 0.65\text{ m}]$ and is surrounded by vertical and horizontal PML domain with a thickness of 0.07 m. For an incoming wave with a frequency of 7497 Hz, the PML domain have a thickness of about 1.5 wavelengths. The domain is discretized with an unstructured grid of 250,000 elements, both triangles and quadrangles. The FW-H integration surface is a cylinder with a radius of 0.2 m, closed in the fore region only for the no-flow condition case. The incoming wave enters from the bypass duct and consists of a (m, μ) duct mode with unit incident intensity. For the no-flow condition, the incoming waves have a frequency of 8282 Hz, which corresponds to a dimensionless frequency of $kr_{\text{fan}} = 21.41$, where $r_{\text{fan}} = 0.14$ m is

Table 2 Short cowl nozzle: mean flow properties at the ducts' inlet

	No flow	Static approach
M_∞	0.000	0.000
M_{fan}	0.000	0.447
M_{turb}	0.000	0.223
c_∞, m/s	340.17	340.17
c_{fan}, m/s	340.17	347.19
c_{turb}, m/s	340.17	527.62
ρ_∞, kg/m^3	1.225	1.225
ρ_{fan}, kg/m^3	1.225	1.177
ρ_{turb}, kg/m^3	1.225	0.509

the radius of the bypass duct at the exit plane. The larger element of the mesh has a characteristic length of about 0.0022 m; therefore, there are at least 19 elements per wavelength. In Fig. 8a the near-field instantaneous pressure perturbations for the duct mode (0, 1) in the no-flow condition is shown, whereas in Fig. 8b the corresponding SPL directivity pattern, describing the field radiated out of the engine, is presented. The far-field directivity is evaluated on an arc with the center defined at the center of the bypass duct exit section and a radius equal to $r = 12$ m. Figures 9a and 9b show similar results for mode (9, 1), always with frequency 8282 Hz. The numerical calculations corresponding to the static-approach condition are shown in Figs. 10 and 11 for modes (0, 1) and (9, 1) with $f = 7497$ Hz ($kr_{\text{fan}} = 19.01$). These calculations were performed on the same grid used for the no-flow condition, resulting in at least 20 elements per wavelength. All the computed cases confirm, as expected, the existence of a direction of maximum intensity of the radiation, ranging from 30 to 60 deg depending upon the mean flow conditions.

The long cowl nozzle is the geometry of the test nozzle used in the TURNEX project's experimental measurements [23,24]. Numerical simulations on this geometry are carried out for two flow conditions, called static approach and static cutback. These flow conditions present a mean velocity both inside the bypass duct and inside the core duct. The flow properties at the ducts' inlet for each flow condition are given in Table 3. Mean flow computations for the long cowl nozzle geometry were performed within the TURNEX project by Rolls-Royce Deutschland (RRD), solving the RANS equations. As an example, Fig. 12 reports the axial velocity contours for the static-approach case. The nodal values of the mean flow on the acoustic mesh are interpolated with the same method used for the short cowl nozzle.

The near-field domain is discretized with an unstructured grid of 275,000 nodes and, in the external region, it extends for $z \in [-0.44\text{ m}; 0.95\text{ m}]$ and for $r \in [0.0\text{ m}; 0.7\text{ m}]$ and is surrounded by vertical and horizontal PML domain with a thickness of 0.08 m. In terms of the wavelengths, assuming a frequency of 7107.5 Hz, the PML domain have a thickness of about 1.7 wavelengths. The FW-H integration surface is a cylinder with a radius of 0.275 m. The incoming waves enter from the bypass duct and consist of a selection of (m, μ) duct modes, which corresponds to the target modes generated during the experiments; the intensity of each mode is given by the experimental measurements. It is important to point out that during the experiments besides the target modes some spurious unwanted modes were also present. However the power ratio of each target mode with respect to the most powerful unwanted mode (TVA, target vs unwanted mode) is, in all the conditions, higher than 10 dB. Therefore, these unwanted modes are not taken into account in the calculations.

In the static-approach condition, the incoming waves have a frequency of 7107.5 Hz, which corresponds to a dimensionless frequency of $kr_{\text{fan}} = 14.44$, where $r_{\text{fan}} = 0.11$ m is the radius of the bypass duct at the exit plane. For this condition the resolution of the mesh is about 21 elements per wavelength. In Figs. 13a, 14a, and 15a, the near-field instantaneous pressure perturbations for duct modes (4, 1), (4, 2), and (4, 3) in the static-approach condition are shown. The corresponding SPL directivity patterns are shown in Figs. 13b, 14b, and 15b. The far-field directivity is evaluated on an arc with a radius of $r = 12$ m and the center placed at the center of the bypass duct exit section. Consistent with the experimental measurements, the calculated directivity is then rescaled to 1 m polar distance from the bypass nozzle exit using the following relation:

$$\text{SPL}_{1\text{ m}} = \text{SPL} + 20\log(r/r_0) \tag{33}$$

where $r_0 = 1$ m.

The three modes are then summed together and the result is compared with the experimental data (see Fig. 16). The superposition is done by evaluating the acoustic quantities for each mode on the FW-H surface, summing up the Fourier coefficients of the modes, and then solving the FW-H equation for the resulting signal. To get a correct superposition of the modes, not only the intensity of each incoming wave must match the experimental data, but also the phase of the corresponding modes must be the same. The final composition is very sensitive with respect to phase errors: a small error in the single mode phase specification may lead to large differences in the final composition. Matching the numerical and experimental data implies that the loudspeaker plane, where the modes are generated in

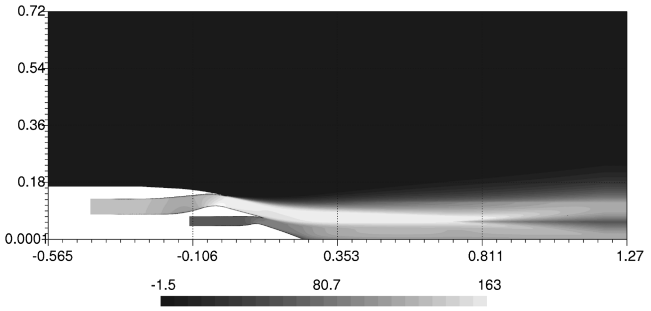

Fig. 7 Short cowl nozzle, mean flow axial velocity [m/s] for static-approach condition (courtesy of the Middle East Technical University).

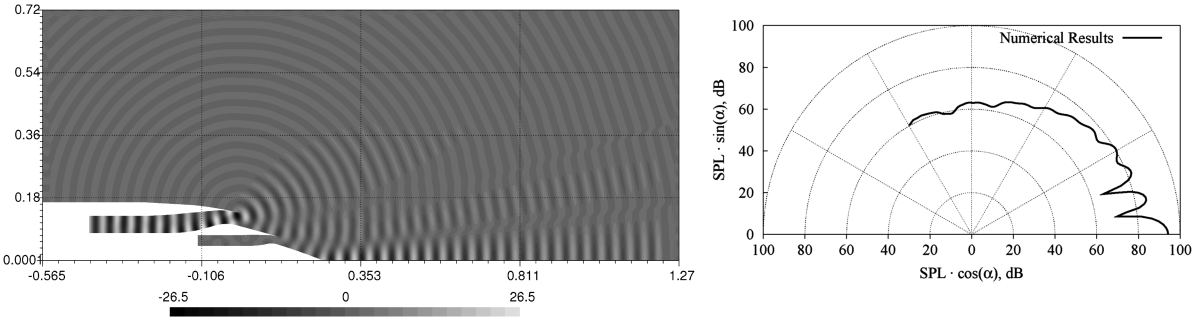

a) b)

Fig. 8 Short cowl nozzle, no-flow condition, mode (0, 1), $f = 8282$ Hz: a) near-field solution: real part of Fourier pressure coefficient, [Pa]; and b) far-field solution: SPL directivity.

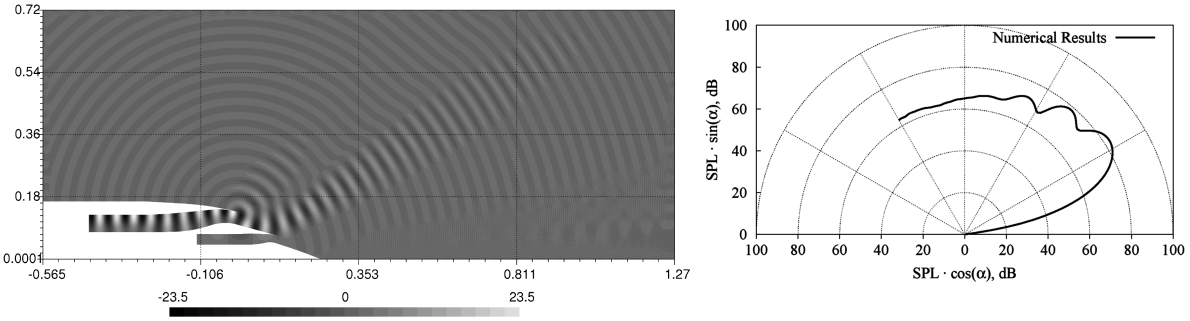

a) b)

Fig. 9 Short cowl nozzle, no-flow condition, mode (9, 1), $f = 8282$ Hz: a) near-field solution: real part of Fourier pressure coefficient, [Pa]; and b) far-field solution: SPL directivity.

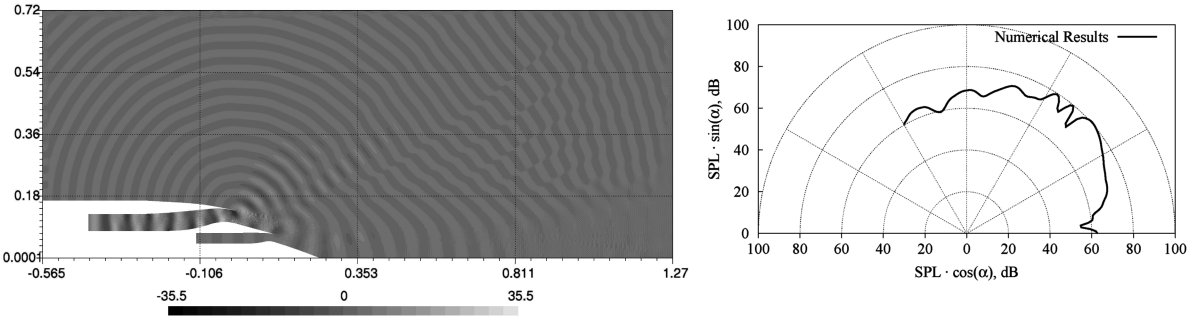

a) b)

Fig. 10 Short cowl nozzle, static-approach condition, mode (0, 1), $f = 7497$ Hz: a) near-field solution: real part of Fourier pressure coefficient, [Pa]; and b) far-field solution: SPL directivity.

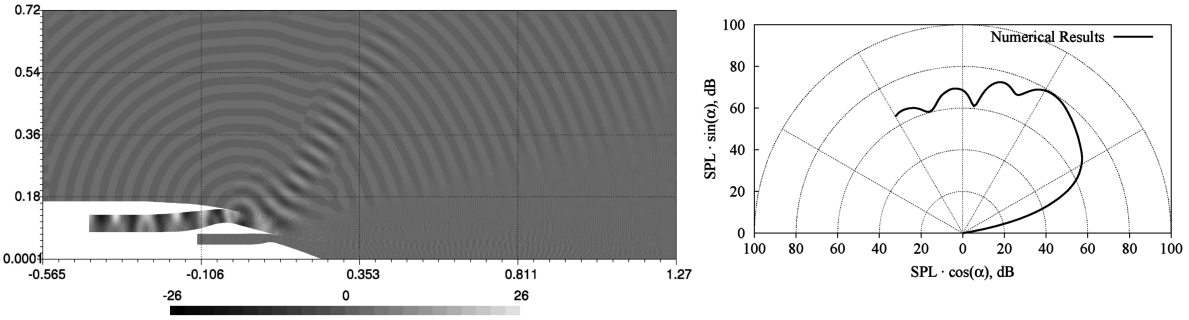

a) b)

Fig. 11 Short cowl nozzle, static-approach condition, mode (9, 1), $f = 7497$ Hz: a) near-field solution: real part of Fourier pressure coefficient, [Pa]; and b) far-field solution: SPL directivity.

Table 3 Long cowl nozzle: mean flow properties at the ducts' inlet

	Static approach	Static cutback
M_∞	0.000	0.000
M_{fan}	0.35	0.43
M_{turb}	0.29	0.44
c_∞, m/s	340.17	340.17
c_{fan}, m/s	353.15	359.74
c_{turb}, m/s	508.75	533.21
$\rho_{f\infty}$, kg/m^3	1.225	1.225
ρ_{rfan}, kg/m^3	1.327	1.434
ρ_{rturb}, kg/m^3	0.598	0.594

the experimental measurements, and the plane where the incoming waves enter in the computational domain must coincide. It has been noted that computational and experimental positions differ by an offset Δz in the z direction, leading to a phase shift of the numerical solution with respect to the experimental results. To correct this mismatch, the numerical solution shown in Fig. 16 is multiplied by a factor $e^{I\Delta z k_z}$, where k_z is the axial wave number of the incoming wave. Experimental data presented in Fig. 16 are measured using two different microphone arrays: the first is an azimuthal ring array with a 9.63 m diameter that could be traversed along the jet axis, whereas the second is a polar arc microphone array arranged in the horizontal plane at rig height with a nominal distance of 12 m to the nozzle exit, covering a range of polar angles in steps of 5 deg from 40 to 120 deg relative to the jet axis. All experimental data were rescaled to 1 m polar distance using Eq. (33). The mismatch between the numerical data and the experimental measurements for the static-approach condition is not yet well understood. As stated earlier, the numerical computation does not include the unwanted modes that were generated during the experiments and this can be one of the causes for

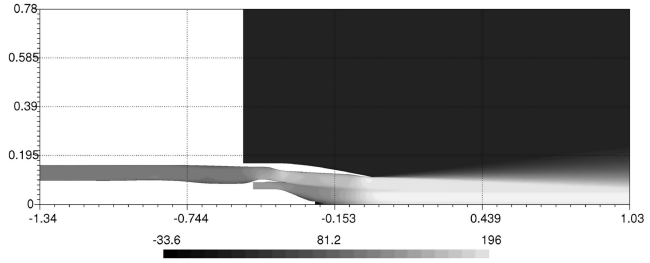

Fig. 12 Long cowl nozzle, mean flow axial velocity [m/s] for static-approach condition (courtesy of Rolls-Royce Deutschland).

the discrepancies. Moreover, it was observed that the superposition of the modes was very sensitive to the offset Δz. Small changes in the value of Δz lead to very different results, leading also to a complete absence of the dip at 70 deg. This suggests that the mismatch between the data is likely due to discrepancies between the phase imposed in the computations and the real phase of the modes.

Figures 17 and 18 show the results for the static-cutback condition. Figure 17 shows the comparison between the numerical results for modes (5, 1), (5, 2), (5, 3), and (5, 4), at a frequency of 9843.75 Hz ($kr_{\text{fan}} = 20.0$ and EPW $= 15$), and the experimental data; the directivity of each single mode is shown in Fig. 17a. For this case, the experimental measurements report an additional, not negligible, incoming wave mode $(-25, 1)$, but the calculations showed that this mode becomes cut off at the reduction of the duct section, which occurs before the bypass duct exit plane. Therefore, mode $(-25, 1)$ does not contribute to the far-field SPL directivity. The last case, with modes (9, 1) and (9, 2), at a frequency of 5742.5 Hz ($kr_{\text{fan}} = 11.67$ and EPW $= 26$), is reported in Fig. 18. For all these results the phase error due to the offset of the loudspeaker plane has been corrected as described earlier. Figure 18 also shows the comparison of the numerical results of the model presented in the paper and the numerical results obtained by the code FLESTURN, developed in the framework of TURNEX at the Middle East Technical University by Özyörük [2]. It solves the LEE in the frequency domain using a fourth-order finite difference scheme.

Taking into account the difficulties of reproducing the exact experimental conditions, the agreement between the numerical results and the experimental data can be considered fairly good. In addition, some of the differences could also be due to the fact that the

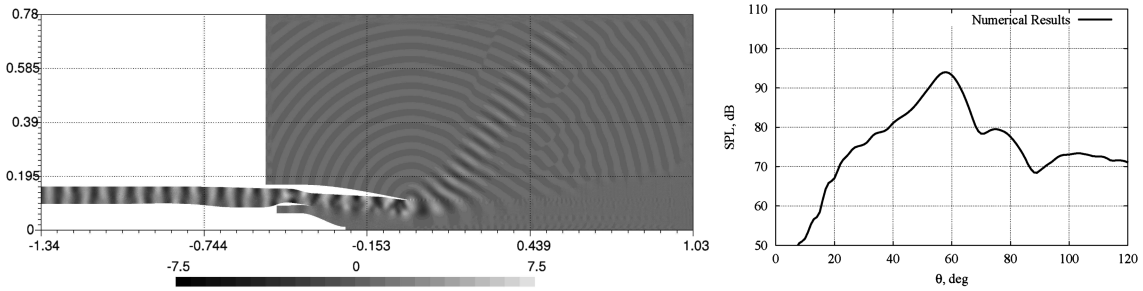

a) b)

Fig. 13 Long cowl nozzle, static-approach condition, mode (4, 1), $f = 7107.5$ Hz: a) near-field solution: real part of Fourier pressure coefficient, [Pa]; and b) far-field solution: SPL directivity.

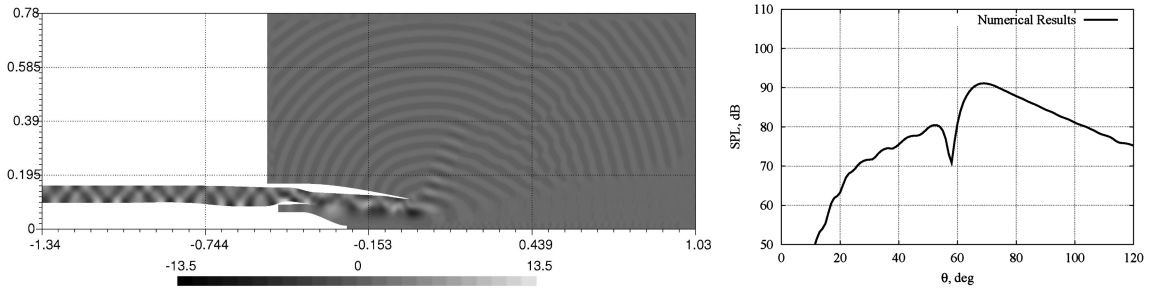

a) b)

Fig. 14 Long cowl nozzle, static-approach condition, mode (4, 2), $f = 7107.5$ Hz: a) near-field solution: real part of Fourier pressure coefficient, [Pa]; and b) far-field solution: SPL directivity.

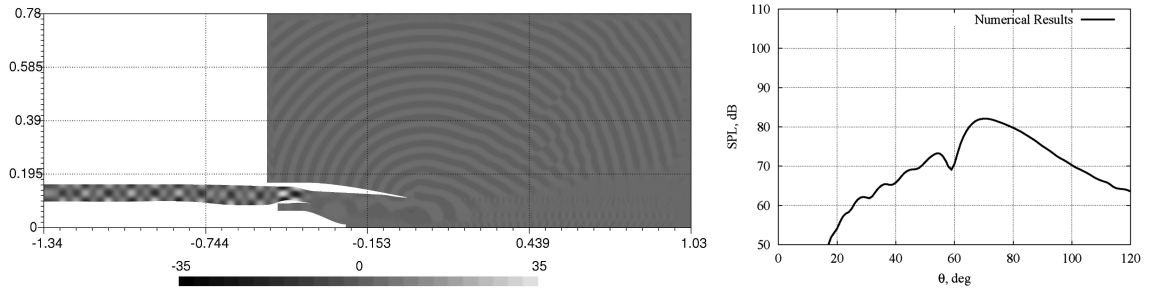

a) b)

Fig. 15 Long cowl nozzle, static-approach condition, mode (4, 3), $f = 7107.5$ Hz: a) near-field solution: real part of Fourier pressure coefficient, [Pa]; and b) far-field solution: SPL directivity.

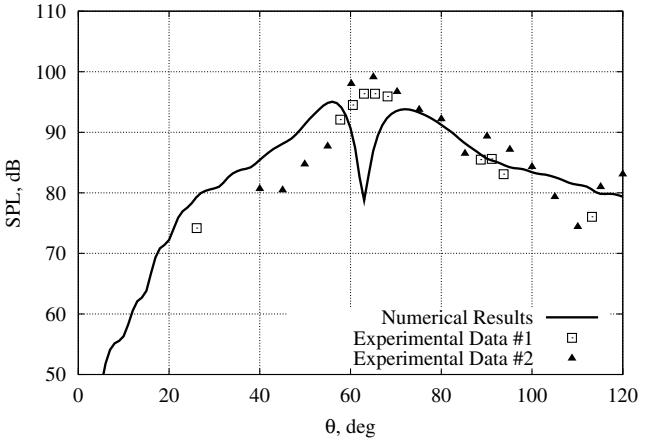

Fig. 16 Long cowl nozzle, static-approach condition, modes (4, 1–3), $f = 7107.5$ Hz. Comparison of superposition of numerical modes and experimental results. Far-field solution, SPL directivity.

present model does not take into account the nonlinear interaction between propagating waves and the turbulent viscous shear layers separating the different streams. For the static-cutback case, the agreement between the two numerical codes is good, except in the low directivity angle zone, where the present code underestimates the SPL. It is possible to state that the proposed numerical model is capable of capturing the main features associated with the sound radiation, such as the direction of maximum intensity in the SPL directivity as well as the overall levels.

IV. Computational Time and Memory Requirements

All the calculations presented in this work were performed on a Linux cluster with three nodes. Each node consists of a two-way dual-core Opteron with 4 GB of RAM; therefore, the cluster has a total of 12 cores and 12 GB of RAM. To calculate the near field with a grid of about 275,000 nodes (that is, 1.1 million unknowns) and a dimensionless frequency equal to $kr = 31.17$, the calculations require about 7.5 min using almost all the RAM of the cluster. Indeed, the limiting factor for these calculations is the RAM requirements: although the MUMPS solver is very efficient, solving a linear system with a direct method requires a large amount of memory. Therefore, with 12 GB RAM, it was possible to solve meshes of up to 275,000 nodes. The code for the far-field calculations is not parallel; despite this, the directivity pattern for each of the presented cases could be obtain in about 3 min.

V. Conclusions

The numerical model based on the solution of the LEE in the frequency domain with a continuous Galerkin FEM, coupled with the FW-H formulation for the evaluation of the far-field directivities, has proved to be a valuable tool for the analysis of the exhaust noise radiation problem. The multifrontal algorithm for the matrix direct inversion MUMPS enables a parallel distribution of the memory requirements. With the LEE it is possible to study acoustic wave propagation in the presence of rotational mean flows. The frequency-domain approach suppress the Kelvin–Helmholtz instability waves, which pollute LEE solutions in time-domain calculations. Moreover, each single calculation, limited to a single frequency, is well suited to the exhaust noise radiation problem in which the incoming wave can

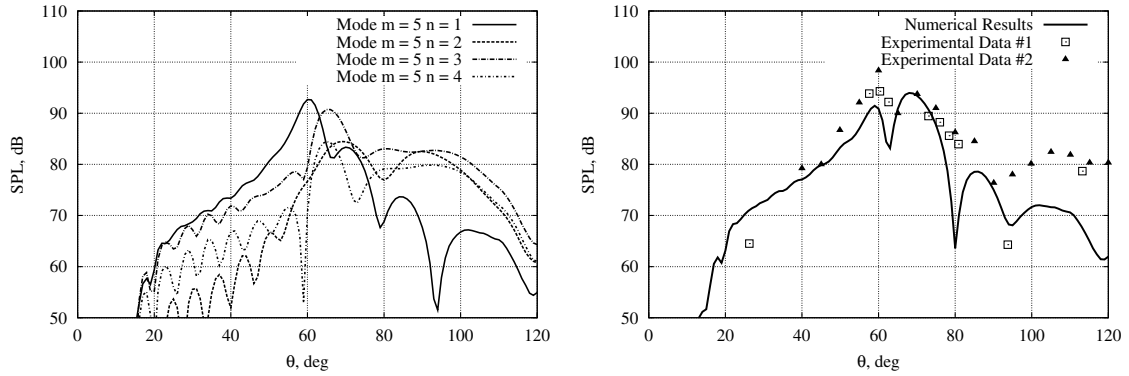

Fig. 17 Long cowl nozzle, static-cutback condition, modes (5, 1–4), $f = 9843.75$ Hz, far-field solution, SPL directivity: a) single modes, and b) comparison of superposition of numerical modes and experimental results.

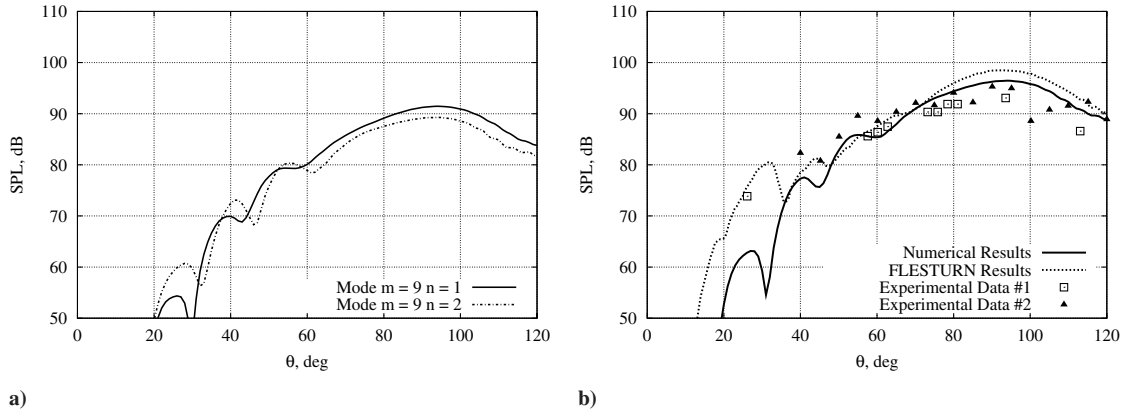

Fig. 18 Long cowl nozzle, static-cutback condition, modes (9, 1–2), $f = 5742.5$ Hz, far-field solution, SPL directivity: a) single modes, and b) comparison of superposition of numerical modes and experimental results.

be treated as a superposition of the elementary duct modes. The model is well suited for design and optimization processes.

The model has been successfully validated with the analytical solution of the Munt problem. In the case of realistic engine configurations, the numerical results reproduce the main expected features. A comparison with the experimental results and numerical computations of a finite difference solution of the LEE is positive. The uncertainties are mainly due to the difficulty in prescribing incoming waves corresponding to the experimental data.

Acknowledgments

This work was supported by the European Commission through the FP6 TURNEX project, coordinated by Brian J. Tester (Technical Officer: Daniel Chiron) and by the Regione Piemonte (Italy) through the GREAT 2020 project. The authors are grateful to the partners of the TURNEX project: Technische Universiteit Eindhoven for providing the analytical results for the Munt problem; Rolls-Royce Deutschland for providing the mean flow data for the long cowl nozzle test case; DLR, German Aerospace Research Center and the Institute of Sound and Vibration Research for the experimental data; and the Middle East Technical University for providing the numerical results for the long cowl nozzle test case and the mean flow data for the short cowl nozzle test case. The authors acknowledge the reviewers for their helpful comments.

References

[1] Agarwal, A., Morris, P., and Mani, R., "The Calculation of Sound Propagation in Nonuniform Flows: Suppression of Instability Waves," *AIAA Journal*, Vol. 42, No. 1, 2004, pp. 80–88. doi:10.2514/1.619

[2] Özyörük, Y., "Numerical Prediction of Aft Radiation of Turbofan Tones Through Exhaust Jets," *Journal of Sound and Vibration*, Vol. 325, Nos. 1–2, 2009, pp. 122–144. doi:10.1016/j.jsv.2009.03.012

[3] Rao, P., and Morris, P., "Use of Finite Element Methods in Frequency Domain Aeroacoustics," *AIAA Journal*, Vol. 44, No. 7, 2006, pp. 1643–1652. doi:10.2514/1.12932

[4] Myers, M., "On the Acoustic Boundary Conditions in the Presence of Flow," *Journal of Sound and Vibration*, Vol. 71, No. 3, 1980, pp. 429–434. doi:10.1016/0022-460X(80)90424-1

[5] Montgomery, D., and Verdon, J., "A Three-Dimensional Linearized Unsteady Analysis for Turbomachinery Blade Rows," NASA CR 4770, 1997.

[6] Hall, K., "A Variational Finite Element Method for Computational Aeroacoustic Calculations of Turbomachinery Noise," *Proceedings of the 2nd CAA Workshop on Benchmark Problems*, CP 3352, NASA, 1997, pp. 269–278.

[7] Amestoy, P., Guermouche, A., L'Excellent, J.-Y., and Pralet, S., "Hybrid Scheduling for the Parallel Solution of Linear Systems," *Parallel Computing*, Vol. 32, No. 2, 2006, pp. 136–156. doi:10.1016/j.parco.2005.07.004

[8] Hu, F. Q., "On Absorbing Boundary Conditions for Linearized Euler Equations by a Perfectly Matched Layer," *Journal of Computational Physics*, Vol. 129, 1996, pp. 201–219. doi:10.1006/jcph.1996.0244

[9] Munt, R., "The Interaction of Sound with a Subsonic Jet Issuing from a Semi-Infinite Cylindrical Pipe," *Journal of Fluid Mechanics*, Vol. 83, No. 4, 1977, pp. 609–640. doi:10.1017/S0022112077001384

[10] Tyler, J., and Sofrin, T., "Axial Flow Compressor Noise Studies," *SAE Transactions*, Vol. 70, 1962, pp. 308–332.

[11] Goldstein, M., *Aeroacoustics*, McGraw–Hill, New York, 1976.

[12] Zhang, X., Chen, X. X., Morfey, C. L., and Tester, B. J., "Computation of Fan Noise Radiation Through a Realistic Engine Exhaust Geometry with Flow," AIAA Paper 2003-3267, May 2003.

[13] Tester, B. J., Gabard, G., and Özyörük, Y., "Influence of Mean Flow Gradients on Fan Exhaust Noise Predictions," , AIAA Paper 2008-2825, May 2008.

[14] Hu, F. Q., "A Stable, Perfectly Matched Layer for Linearized Euler Equations in Unsplit Physical Variables," *Journal of Computational Physics*, Vol. 173, 2001, pp. 455–480. doi:10.1006/jcph.2001.6887

[15] Astley, R. J., Walkington, N. J., and Eversman, W., "Accuracy and Stability of Finite Element Schemes for the Duct Transmission Problem," *AIAA Journal*, Vol. 20, No. 11, 1982, pp. 1547–1556. doi:10.2514/3.51219

[16] Codina, R., "On Stabilized Finite Element Methods for Linear Systems of Convection-Diffusion-Reaction Equations," *Computer Methods in Applied Mechanics and Engineering*, Vol. 188, 2000, pp. 61–82. doi:10.1016/S0045-7825(00)00177-8

[17] Guasch, O., and Codina, R., "An Algebraic Subgrid Scale Finite Element Method for the Convected Helmholtz Equation in Two Dimensions with Applications in Aeroacoustics," *Computer Methods in Applied Mechanics and Engineering*, Vol. 196, 2007, pp. 4672–4689. doi:10.1016/j.cma.2007.06.001

[18] Ffowcs Williams, J., and Hawkings, D., "Sound Generation by Turbulence and Surfaces in Arbitrary Motion," *Proceedings of the Royal Society A Mathematical Physical And Engineering Sciences*, Vol. 264, No. 1151, 1969, pp. 321–342. doi:10.1098/rsta.1969.0031

[19] Lockard, D. P., "An Efficient, Two-Dimensional Implementation of the Ffowcs Williams And Hawkings Equation," *Journal of Sound and Vibration*, Vol. 229, No. 4, 2000, pp. 897–911. doi:10.1006/jsvi.1999.2522

[20] Rienstra, S. W., "Acoustic Radiation From a Semi-Infinte Annular Duct in a Uniform Subsonic Mean Flow," *Journal of Sound and Vibration*, Vol. 94, No. 2, 1984, pp. 267–288. doi:10.1016/S0022-460X(84)80036-X

[21] Gabard, G., and Astley, R., "Theoretical Model for Sound Radiation from Annular Jet Pipes: Far- and Near-Field Solutions," *Journal of Fluid Mechanics*, Vol. 549, 2006, pp. 315–341. doi:10.1017/S0022112005008037

[22] Demir, A., and Rienstra, S., "Sound Radiation from an Annular Duct with Jet Flow and a Lined Centerbody," AIAA Paper 2006-2718, May 2006.

[23] Arnold, F., Tapken, U., Bauers, R., and Zillmann, J., "Turbomachinery Exhaust Noise Radiation Experiments—Part 1 Polar Directivity Measurements," AIAA Paper 2008-2857, May 2008.

[24] Tapken, U., Bauers, R., Arnold, F., and Zillmann, J., "Turbomachinery Exhaust Noise Radiation Experiments—Part 2 In-Duct and Far-Field Mode Analysis," AIAA Paper 2008-2858, May 2008.

J. Astley
Associate Editor